Small

NANO · MICRO small
www.small-journal.com

RESEARCH ARTICLE OPEN ACCESS

Engineering Proton Conductive Metal–Organic Glasses Through Secondary Network Formers

Nattapol Ma[1] | Hideka Ando[1] | Renzhi Ma[2] | Takashi Nakanishi[2]

[1]International Center for Young Scientists (ICYS), National Institute for Materials Science, Tsukuba, Ibaraki, Japan | [2]Research Center for Materials Nanoarchitectonics (MANA), National Institute for Materials Science, Tsukuba, Ibaraki, Japan

Correspondence: Nattapol Ma (ma.nattapol@nims.go.jp)

Received: 21 November 2025 | **Revised:** 8 February 2026 | **Accepted:** 9 February 2026

Keywords: amorphous materials | coordination polymers | metal–organic frameworks | proton conductivities | secondary network formers

ABSTRACT

Crystal–liquid–glass phase transitions in coordination polymers (CPs) and metal–organic frameworks (MOFs) have opened new opportunities for materials processing and for accessing novel or enhanced functionalities inherited from their crystalline precursors. However, strategies to modulate the properties of the resulting glassy states, collectively referred to as metal–organic glasses (MOGs), have primarily relied on crystal engineering. Such approaches face intrinsic limitations, as the rare occurrence of melting behavior in CPs/MOFs and the narrow compositional windows that sustain a stable liquid phase restrict access to new structures and properties. Inspired by the compositional tunability of conventional oxide glass, this work explores a strategy to modulate MOG properties by incorporating inorganic zirconium hydrogen phosphate as a secondary network former. We hypothesize that the mismatch between tetrahedrally coordinated Zn^{2+} in the parent MOG and octahedrally coordinated Zr^{4+} in the additive induces distinct structural and functional modifications. By systematically varying the content of the zirconium hydrogen phosphate, we demonstrate a linear increase in the glass transition temperature, viscosity, and anhydrous proton conductivity, reaching 2.6 mS cm^{-1} at 150°C. These results highlight the potential of translating design principles from inorganic glass science to fine-tune the properties of MOGs.

1 | Introduction

The recent discovery of crystal–liquid–glass phase transitions in coordination polymers (CPs) and metal–organic frameworks (MOFs) has opened new opportunities for materials processing and for accessing novel or enhanced functionalities derived from their crystalline precursors [1–3]. This concept has attracted significant attention, motivating a growing effort to identify new meltable CPs/MOFs with unique properties [4, 5]. To date, however, strategies to modify the properties of the glassy states of CPs/MOFs, collectively referred to as metal–organic glasses (MOGs), have primarily relied on crystal engineering. In this approach, CPs/MOFs are first designed in their crystalline form with the expectation that targeted functionalities will persist after melt-quenching [6, 7]. Yet, the rarity of melting behavior in CPs/MOFs, observed in less than 1% of known CPs/MOFs [5, 8], and the narrow compositional windows that support a stable liquid state impose intrinsic limitations on the accessible properties of MOGs. For instance, among the series $M(H_2PO_4)_2$(1,2,4-triazole)$_2$ (M = Zn^{2+}, Cd^{2+}, Mn^{2+}, Co^{2+}, Fe^{2+}, Cr^{2+}), only the Zn^{2+} analogue melts upon heating, while the others remain crystalline until thermal decomposition [9–12]. Developing approaches that allow direct tuning of MOG properties, without requiring the synthesis of new meltable crystals, would therefore greatly expand the design space and unlock broader applications, particularly for systems in which crystal-to-glass transitions are difficult to achieve.

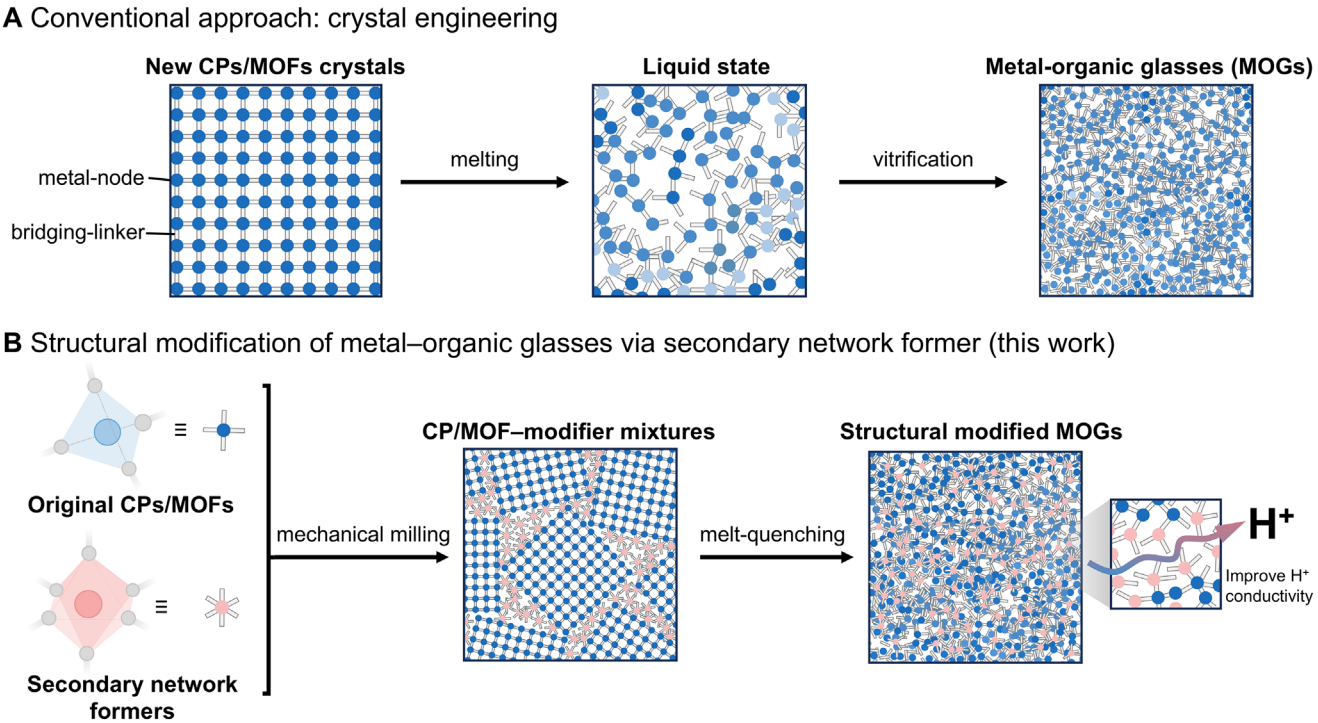

FIGURE 1 | Schematic illustration of (A) conventional approach in metal–organic glass properties modifications via crystal engineering and (B) the proposed structural modification process via secondary network former addition in this work.

To date, controlling MOG properties, including viscosity [13], thermal behavior [7], mass and ion transport [14], mechanical properties [15], optics [16] and magnetics [17] responses, and beyond, remains a central challenge, as only a small number of CPs/MOFs can form stable liquids upon heating (Figure 1A). Even slight modifications in crystal composition potentially cause the material to retain its crystalline state up to the decomposition temperature, rather than melting [9, 11, 18]. This contrasts sharply with conventional oxide glasses, where property control is rarely achieved by designing new crystalline precursors. Instead, oxide glass networks are continuously tuned through compositional modification with network modifiers, secondary network formers (intermediates), and other additives [19, 20]. Such compositional flexibility enables the formation of an enormous diversity of oxide glasses with tunable atomic structures and physical properties, including transparency, chemical durability, and mechanical strength, supporting applications ranging from architectural glass [21] to nuclear waste immobilization [22]. Inspired by the success in oxide glasses, recent studies have explored the use of "network modifiers" in MOGs to induce depolymerization and chain fragmentation through ligand exchanges, thereby reducing viscosity or altering thermal behavior in selected systems such as zinc–phosphate–azole CPs [23, 24], metal-bis(acetamides) [25], and zeolite imidazolate frameworks [13]. However, composition tuning in glasses is not limited to depolymerization. It can also involve incorporating "secondary network formers" or "intermediates" that participate in network formation (polymerization), thereby enhancing structural stability or introducing new physical properties through cross-linking or charge compensation of modifier ions [26]. Yet, to date, no examples of MOG property modulation through the incorporation of such secondary network formers or intermediates have been reported.

In this article, we present a strategy to modulate the thermal properties, viscosity, and anhydrous proton conductivity of a representative zinc–phosphate–azole-based MOG through the systematic incorporation of zirconium hydrogen phosphate, which potentially acts as a secondary network former (Figure 1B). This role is analogous to that of Al_2O_3 as a network-forming oxide in conventional silica-based glasses. We hypothesize that introducing octahedrally coordinated Zr^{4+} into the tetrahedrally coordinated Zn^{2+} chains of the parent MOG introduces additional phosphate sites, which facilitate polymerization and strengthen hydrogen-bonding connectivity (Figure 2A). These structural modifications are expected to influence the macroscopic properties of the resulting glasses strongly. We demonstrate that the glass transition temperature, viscosity, and anhydrous proton conductivity can all be tuned through compositional control. Synchrotron X-ray total scattering, pair distribution function (PDF) analysis, thermal and rheological measurements, and positron annihilation lifetime spectroscopy (PALS) reveal property trends consistent with the behavior typically associated with secondary network formers in conventional oxide glasses, thereby enabling direct compositional tuning of the glasses' macroscopic properties.

2 | Results and Discussion

2.1 | Synthesis, Melting Behavior, and Glass Formation

A representative CP, $[Zn(HPO_4)(H_2PO_4)_2](H_2Im)_2$ (HIm = imidazole, Figure S1), was selected because it forms a stable liquid state and is broadly compatible with functional dopants [23, 27]. The compound, hereafter referred to as ZnPIm, was synthesized

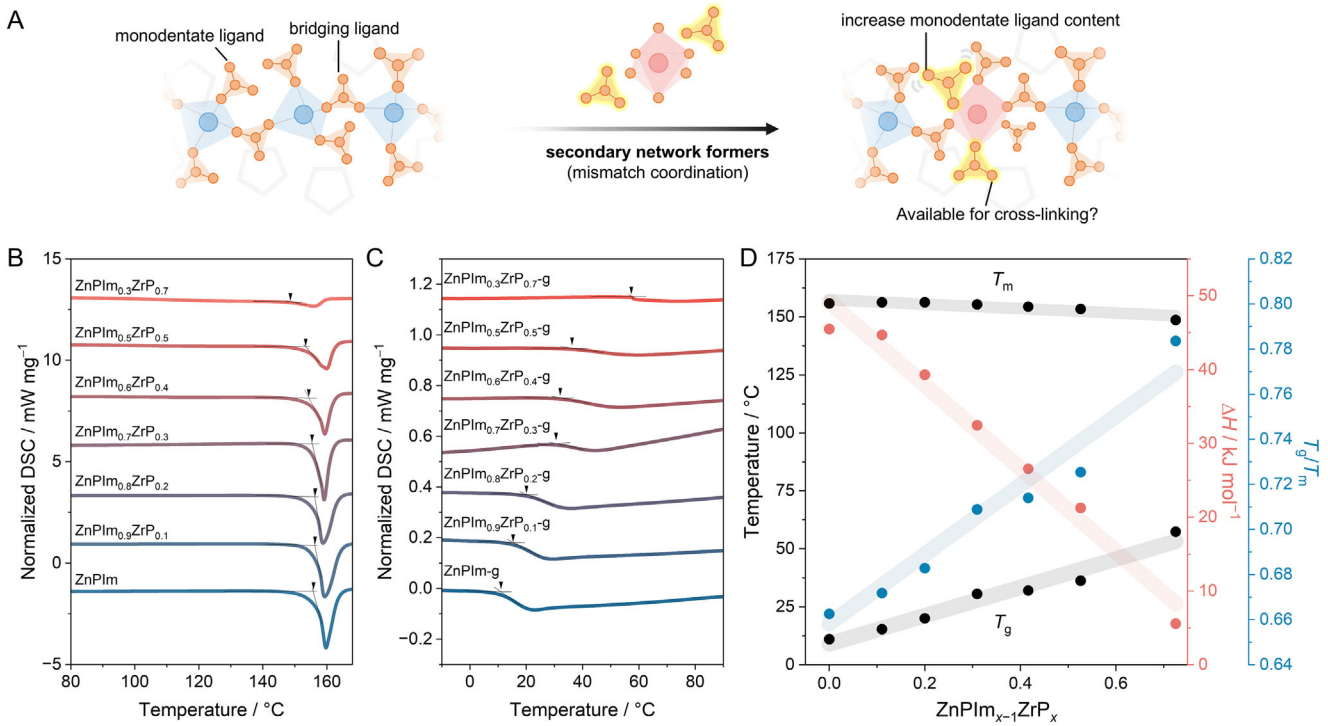

FIGURE 2 | (A) Schematic illustration of the hypothesized structure tuning in metal–organic glasses through the incorporation of secondary network formers. (B) First and (C) second heating DSC profiles of all samples under N_2 atmosphere measured at a heating rate of 10°C min^{-1}. (D) Variation of melting temperature (T_m), glass transition temperature (T_g), enthalpy change (ΔH), and the T_g/T_m ratio as a function of the mole fraction (x) of ZrP in $ZnPIm_{1-x}ZrP_x$.

on the gram scale following previously reported procedures (see detailed method in Supporting Information) [23, 27]. ZnPIm consists of 1D chains of tetrahedrally coordinated Zn^{2+} ions bridged by orthophosphate (HPO_4^{2-}). Two additional monocoordinated $H_2PO_4^-$ anions complete the coordination sphere. Charge neutrality is maintained by two interchain imidazolium cations per Zn^{2+}. The powder X-ray diffraction (PXRD) pattern of the as-synthesized ZnPIm matched well with the simulated pattern (Figure S2). Heating ZnPIm above its onset melting temperature (T_m = 155.7°C) resulted in crystal melting (Figure 2B,C; Figure S3). The liquid phase remained stable up to ca. 195°C, beyond which thermal decomposition began. Cooling the melts prior to decomposition yielded a vitrified glassy state, denoted ZnPIm-g. Upon reheating, differential scanning calorimetry (DSC) confirmed an onset glass transition temperature (T_g) of 11.0°C. At room temperature (25°C), ZnPIm-g remains a practically stable, highly viscous supercooled liquid, showing no signs of crystallization even at a slow DSC scan rate of 0.5°C min^{-1} up to 160°C (Figure S4) [28]. Further details of temperature-dependent viscosity are discussed in the viscoelasticity section.

Amorphous zirconium hydrogen phosphate with the formula $Zr(HPO_4)_2{\bullet}nH_2O$ (ZrP) was selected as an additive and is expected to act as a secondary network former (Figure S5). The amorphous nature of ZrP is expected to diminish interfacial mismatch in comparison to its crystalline counterparts. The short-range structure of ZrP closely resembles that of γ-$Zr(H_2PO_4)(PO_4){\cdot}2H_2O$ (γ-ZrP), as confirmed by pair distribution function analysis (Figures S6–S8) [29]. Further details of this technique will be discussed in a later section. The crystalline γ-phase consists of octahedrally coordinated Zr^{4+} ions, each bound to two $H_2PO_4^-$ and four distinct PO_4^{3-} groups. Upon heating to 1200°C under N_2 atmosphere during thermogravimetric analysis (TGA), ZrP exhibits continuous weight loss, reaching a total of ~14.95% (see details in Figure S10). This weight loss is attributed to the removal of one water molecule per $Zr(HPO_4)_2$ unit via phosphate condensation [30, 31], while the remaining loss is assigned to residual water in the ZrP. Based on these observations, the composition of ZrP was estimated to be $Zr(HPO_4)_2{\bullet}1.6H_2O$.

Preparation of modified MOGs began by homogenizing as-synthesized ZnPIm and ZrP at different mole ratios using a mixer mill operated at 15 Hz for 10 min (Figure 1B). The resulting mixtures are referred to as $ZnPIm_{1-x}ZrP_x$, where x represents the mole fraction of ZrP (x = 0.1, 0.2, 0.3, 0.4, 0.5, and 0.7) (Figure S12). PXRD patterns of all mixtures closely resembled that of ZnPIm, with no evidence of ZrP crystallization (Figure S13). The actual Zr to Zn mole fractions of all samples were analyzed by inductively coupled plasma optical emission spectroscopy (ICP-OES, Table S1). The thermal stability of the mixtures was comparable to that of ZnPIm. However, samples with higher ZrP content exhibited greater weight loss below 200°C, attributed to the release of ZrP's water molecules (Figures S14–S20).

Upon heating at 10°C min^{-1}, DSC profiles of all partially dehydrated samples (see the detailed method in the Supporting Information) exhibited a single endothermic melting peak, with onset T_m ranging from 148.7°C to 156.3°C (Figure 2B,D; Table S2). This variation in T_m is considerably smaller than that typically observed in systems displaying eutectic behavior [23] or flux

melting [24], as previously reported for the Zn-azole-phosphate CP family. The total enthalpy change (ΔH) associated with melting decreased progressively with increasing ZrP content, from 45.5 kJ mol^{-1} for ZnPIm-g to 5.6 kJ mol^{-1} for $ZnPIm_{0.3}ZrP_{0.7}$. This trend is consistent with the reduced fraction of meltable ZnPIm in the mixtures. When the ΔH is normalized to the mole fraction of ZnPIm in each sample, the value initially increases from 45.5 kJ mol^{-1} for ZnPIm to 50.2 kJ mol^{-1} for $ZnPIm_{0.9}ZrP_{0.1}$ before gradually decreasing to 44.8 kJ mol^{-1} for $ZnPIm_{0.5}ZrP_{0.5}$. The increase in the normalized ΔH relative to pristine ZnPIm suggests the dissolution event of ZrP into the ZnPIm melts. At higher ZrP contents, the normalized ΔH further decreases to 20.3 kJ mol^{-1} for $ZnPIm_{0.3}ZrP_{0.7}$ (Table S2). This reduction likely stems from differences in the extent of mechanically induced amorphization of ZnPIm during the milling process, particularly in ZrP-rich systems [32–34]. This observation is supported by the decreasing crystallinity levels derived from the PXRD data of the $ZnPIm_{1-x}ZrP_x$ samples (Figure S21).

Subsequent DSC heating measurements revealed a single glass transition for all samples (Figure 2C; Figure S22–S28) [35]. The melt-quenched materials are hereafter denoted as $ZnPIm_{1-x}ZrP_x$-g, and T_g values are reported as onset temperatures. A linear increase in T_g was observed with higher ZrP content, increasing from 11.0°C for ZnPIm-g to 57.4°C for $ZnPIm_{0.3}ZrP_{0.7}$-g (Figure 2D; Table S2). Correspondingly, the T_g/T_m ratio (based on absolute temperature), an indicator that reflects the tendency of a liquid to form a glass upon cooling rather than crystallizing [36, 37], also increases linearly with ZrP content, from 0.66 for ZnPIm-g to 0.78 for $ZnPIm_{0.3}ZrP_{0.7}$-g. This increase in T_g contrasts with all previous examples in other MOG systems, where additives typically act as network modifiers, promoting chain fragmentation and thereby lowering the T_g of the parent compounds [13, 24, 25]. Binary glass systems composed of MOG constituents generally exhibit either a weighted-average T_g in homogeneously mixed glasses [38, 39], or distinct T_g values corresponding to the individual parent components in phase-separated systems [40]. The effect of ZrP observed here more closely resembles that of Al^{3+} as a secondary network former or intermediate in Na_2O–Al_2O_3–SiO_2 glasses, where increasing Al^{3+} content promotes the degree of polymerization (or cross-linking) and, consequently, raises T_g [26]. In addition, the heat capacity change at T_g (ΔC_p) decreases with increasing ZrP content (Figures S29 and S30), suggesting enhanced network rigidity and a reduced configurational degree of freedom above T_g [26, 41].

To verify that the observed increase in T_g arises from ZrP and parallels the effect typically observed when adding secondary network formers in conventional oxide glasses, a control experiment was conducted using Al_2O_3 as a chemically inert additive. Under the relatively mild melting conditions employed in this work (< 175°C), Al_2O_3 remains unreactive. This contrasts with aluminosilicate glass systems, which require processing temperatures above 1100°C [26]. An equimolar mixture of ZnPIm and Al_2O_3 was prepared following the same synthetic procedure, yielding $ZnPIm_{0.5}[Al_2O_3]_{0.5}$ (Figure S31). The DSC profile of $ZnPIm_{0.5}[Al_2O_3]_{0.5}$ exhibits a single endothermic peak of melting (T_m) at 159.2°C (Figure S32). More importantly, the T_g of the melt-quenched sample ($ZnPIm_{0.5}[Al_2O_3]_{0.5}$-g) remained essentially unchanged at 10.5°C, compared to 11.0°C of the ZnPIm-g. This value is significantly lower than the 36.3°C observed for $ZnPIm_{0.5}ZrP_{0.5}$-g with comparable additive contents, suggesting that the higher T_g potentially arises from the contribution of ZrP, rather than from the mere presence of an inert additive.

2.2 | Morphology and Free Volume of MOGs

Modified MOGs were prepared on a larger scale by heating $ZnPIm_{1-x}ZrP_x$ under an inert Ar atmosphere at 175°C for 10 min (see the detailed method in the Supporting Information), then allowing it to cool naturally to room temperature (Figure S33). This process yielded amorphous solids that exhibited broad diffuse scattering features in their XRD patterns, confirming the absence of long-range order (Figure S34). Thermogravimetric analysis results for all modified MOGs prepared by melting at 170°C under N_2 atmosphere show less than 1% weight loss up to at least 190°C (Figures S35–S41). A lower overall weight loss at 500°C was also observed with increasing ZrP content. Additionally, TGA results to 1200°C of all modified MOGs suggest that any residual water after melt-quenching is below the detection limit of TGA-based analysis (Figure S42 and Table S3). Fourier transform infrared (FTIR, Figure S43) spectra of representative $ZnPIm_{0.8}ZrP_{0.2}$-g are largely identical to those of ZnPIm-g, indicating that the imidazole molecules remain protonated and do not coordinate to either Zn^{2+} or Zr^{4+} ions in the melt-quenched MOGs. The observed water-related signals are attributed to the hygroscopic nature of the samples, since FTIR measurements were performed under ambient conditions. Scanning electron microscopy (SEM, Figures S44–S51) revealed smooth, grain-boundary-free surfaces with no evidence of phase segregation from ZnPIm-g up to $ZnPIm_{0.6}ZrP_{0.4}$-g in micrometer length scale. Within this composition range, energy-dispersive X-ray (EDX, Figures S52–S57) mapping further confirmed that both constituents were homogeneously distributed throughout the observed regions. At higher ZrP contents, specifically in $ZnPIm_{0.5}ZrP_{0.5}$-g and $ZnPIm_{0.3}ZrP_{0.7}$-g, distinct Zn- and Zr-rich domains become clearly visible, with the distinction between them becoming increasingly pronounced as the ZrP concentration increases. The melt-quenched samples remain amorphous for at least 2 weeks under ambient conditions, as confirmed by the absence of Bragg peaks in the PXRD patterns (Figure S58).

We further utilized positron annihilation lifetime spectroscopy (PALS, Figure 3) to monitor changes in the pore radius of the free volume within the modified MOGs, providing an indirect assessment of phase segregation and local structures. The lifetime (τ_3) and relative intensity (I_3) of the longest-lived component, orthopositronium (*o*-Ps), are correlated with the average pore (cavity) radius and the relative number of cavities, respectively [42]. Consequently, these parameters reflect the distribution of free spaces within the samples. Mismatched interfaces between segregated phases are expected to generate interfacial cavities, thereby increasing the overall cavity size in the samples [12, 43]. The estimated pore radii (and τ_3) for pure ZnPIm-g and ZrP are 0.241 nm (1.56 ns) and 0.286 nm (2.00 ns), respectively. In the modified MOGs, the free volume decreases below that of pristine ZnPIm-g for compositions of $ZnPIm_{1-x}ZrP_x$-g with $x < 0.5$, suggesting enhanced miscibility between the two components [44]. When $x > 0.5$, the free volume begins to increase again, consistent with the phase segregation observed in the SEM images of

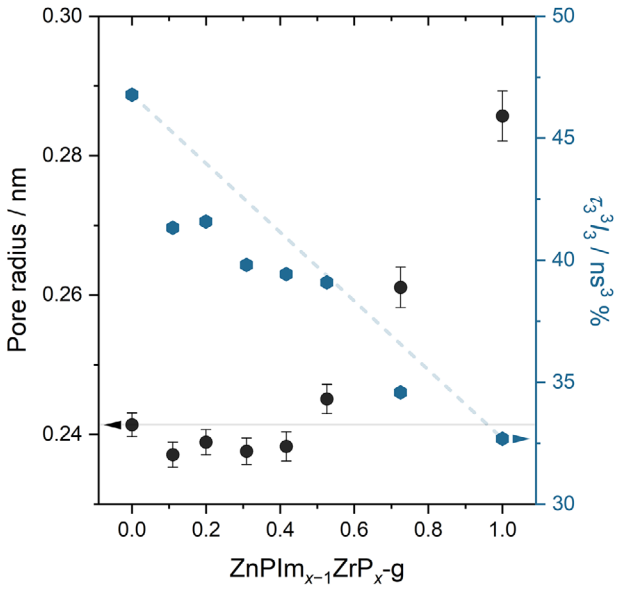

FIGURE 3 | Pore radius as a function of composition of ZnPIm$_{1-x}$ZrP$_x$-g and PALS parameter ($\tau_3{}^3I_3$). These cavity sizes were derived from the orthopositronium (*o*-Ps) lifetime component (τ_3) obtained via Positron Annihilation Lifetime Spectroscopy (PALS). The black line and blue dashed line represent the pore radius value of ZnPIm-g and linear additive fractional free volume reference lines, respectively. See Figure S59 for the PALS spectra and Table S4 for the complete parameters.

ZnPIm$_{0.5}$ZrP$_{0.5}$-g and ZnPIm$_{0.3}$ZrP$_{0.7}$-g. Furthermore, the PALS-derived free volume parameter ($\tau_3{}^3I_3$) as a function of MOG composition displays a sub-additive trend across all compositions. This behavior indicates that the reduced free volume limits overall molecular mobility, thereby restricting local conformational rearrangements [28, 45]. Consequently, the observed increase in T_g with increasing ZrP content, as determined by DSC, can be attributed to the restricted molecular mobility arising from decreased free volume.

2.3 | Short-to-Intermediate Range Structure

The influence of ZrP incorporation on the short- to intermediate-range structure of the modified MOGs was investigated using X-ray total scattering and pair distribution function (PDF) analyses (Figure 4). This technique provides real-space structural information by quantifying the probability of finding atomic pairs at specific interatomic distances, represented as weighted histograms of atom–atom correlations [46]. All samples were characterized both before and after the melt-quenching process. The peak assignments here were confirmed by calculated partial PDFs derived from single-crystal structures of ZnPIm and γ-ZrP (Figures S7 and S60) [29, 47, 48]. Prior to melt-quenching, the PDF profiles of the mixtures closely resembled a superposition of the parent ZnPIm and ZrP components, with relative peak intensities varying according to the composition of each constituent (Figure 4; Figure S61). In the mixed samples, a new peak was observed at approximately 5.6 Å (marked by the red dashed line), located between the characteristic 5.2 and 5.8 Å features of ZrP and ZnPIm, respectively, corresponding to the Zr···Zr$_1$ and Zn···Zn correlations (metal–ligand–metal connectivity). However, the origin of this feature cannot be unambiguously assigned based on the present data.

After melt-quenching, the reciprocal-space total scattering structure factor, $S(q)$, showed the disappearance of Bragg peaks, confirming the transformation to an amorphous phase (Figures S62–S68). The PDF features of the resulting modified MOGs remain largely consistent with those of their parent mixtures at pair distances below approximately 6.5 Å, but with reduced amplitudes. This observation indicates partial preservation of short-range metal–ligand–metal connectivity, including Zr···Zr and Zn···Zn, consistent with the retention of local coordination networks. At shorter pair distances (below 3.5 Å), the PDF features are nearly identical to those observed before melt-quenching, confirming the retention of the local tetrahedral and octahedral coordination geometries around Zn^{2+} and Zr^{4+} centers [24]. At longer pair distances (above 7 Å), the pronounced broadening of the PDF peaks signifies the loss of long-range structural order accompanying vitrification [49]. ^{91}Zr solid-state nuclear magnetic resonance (NMR) reveals subtle differences between pristine ZrP and melt-quenched ZnPIm$_{0.5}$ZrP$_{0.5}$-g, suggesting modest changes in the local environment around the Zr^{4+} centers (Figure S77) [50]. However, further interpretation is limited by the relatively broad NMR signals. Based on structural characterization, ZnPIm-g and ZnPIm$_{0.8}$ZrP$_{0.2}$-g were chosen as representative samples for further characterization to assess how ZrP incorporation affects the viscoelastic and proton-conducting behaviors of the samples.

2.4 | Viscoelasticity

The influence of ZrP on mechanical response was studied by comparing ZnPIm-g and ZnPIm$_{0.8}$ZrP$_{0.2}$-g samples using rheological analysis. Temperature-dependent dynamic mechanical analysis (DMA) and viscosity measurements were conducted to examine the softening behavior upon heating. Two distinct viscoelastic regions were identified, as indicated by the dashed lines in Figure 5A,B [51]. At lower temperatures, both samples exhibit solid-like elasticity, with a nearly constant storage modulus (G'') exceeding the loss modulus (G'). Upon heating, softening begins at approximately 12.3°C for ZnPIm-g and 36.4°C for ZnPIm$_{0.8}$ZrP$_{0.2}$-g. Further heating to above the main relaxation temperature (T_α), at 30.4°C for ZnPIm-g and 60.8°C for ZnPIm$_{0.8}$ZrP$_{0.2}$-g, leads to a transition into viscous, liquid-like behavior. The pronounced increase in both softening and relaxation temperatures in ZnPIm$_{0.8}$ZrP$_{0.2}$-g demonstrates that ZrP incorporation enhances network rigidity, thereby stabilizing solid-like behavior at elevated temperatures. Note that the T_α value is frequency dependent [52].

Temperature-dependent viscosity profiles of both ZnPIm-g and ZnPIm$_{0.8}$ZrP$_{0.2}$-g follow the Mauro-Yue-Ellison-Gupta-Allan (MYEGA) equation (Figure 5C; Table S5) [58]. The glass transition temperatures derived from the viscosity curves ($T_{g,\eta}$) were estimated by extrapolating the viscosity to 10^{12} Pa•s. [58, 59] A distinct increase in $T_{g,\eta}$ was observed, from 6.5°C for ZnPIm to 31.5°C for ZnPIm$_{0.8}$ZrP$_{0.2}$-g, consistent with the trend observed in DSC experiments of the modified MOGs. Throughout the measurement range, the viscosity profile of ZnPIm$_{0.8}$ZrP$_{0.2}$-g

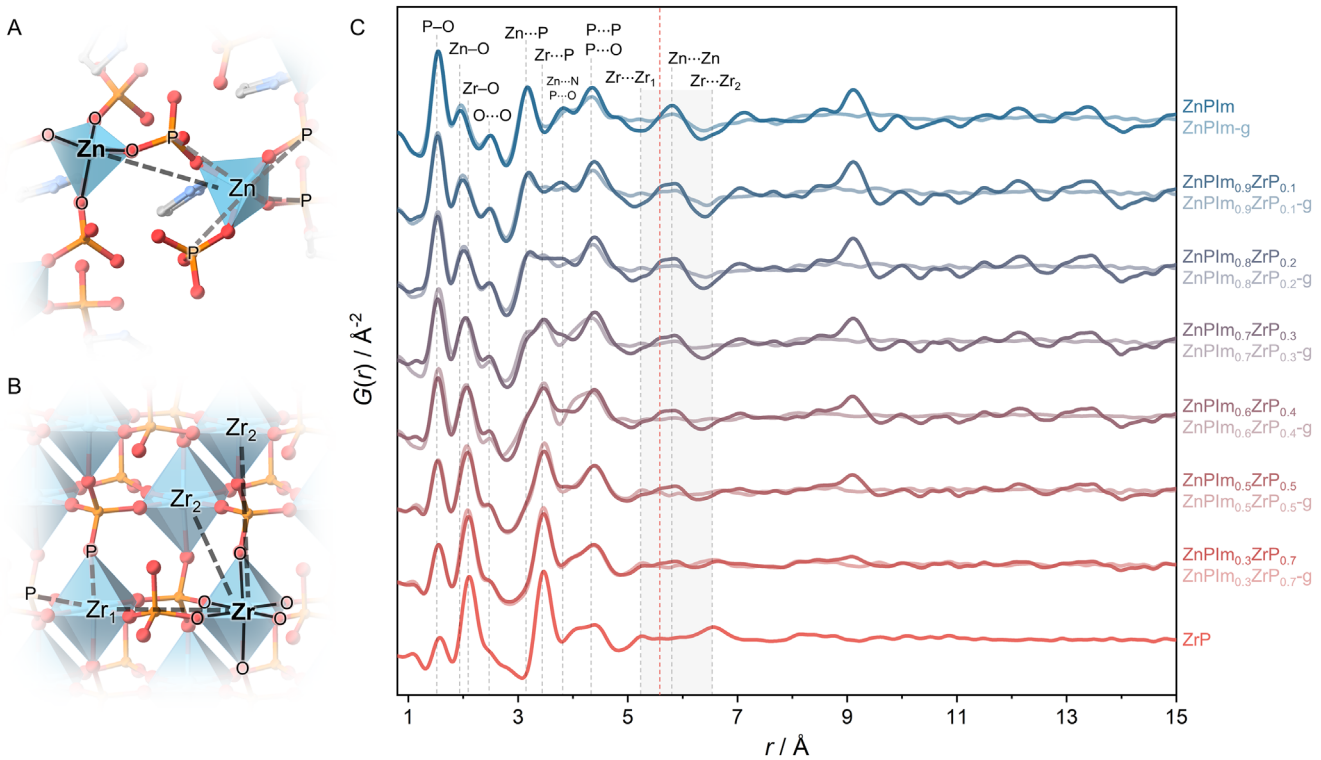

FIGURE 4 | Local structures and pair distribution functions (PDFs) of modified samples. (A) Local coordination environment and pair-distance labeling around (A) Zn^{2+} in ZnPIm and (B) Zr^{4+} in γ-ZrP. Zn and Zr are shown as polyhedra, while P, O, C, and N atoms are represented in orange, red, gray, and light blue, respectively. (C) Experimental PDFs of ZnPIm, ZrP, and a series of $ZnPIm_{1-x}ZrP_x$ samples and their melt-quenched counterparts, ZnPIm-g and $ZnPIm_{1-x}ZrP_x$-g. Peak labels are assigned based on partial PDFs (Figures S7 and S60) simulated from crystal structures of γ-ZrP [29] and ZnPIm [47]. Additional S(q) data and extended PDF data up to 30 Å are provided in Figures S8 and S62–S76.

shifts markedly toward higher temperatures. For example, the temperature at which the viscosity reaches the standard working point ($\eta = 10^3$ Pa•s) increases from 73°C for ZnPIm-g to approximately 109°C for $ZnPIm_{0.8}ZrP_{0.2}$-g. At these temperatures, the viscosity of both samples is comparable to molten soda-lime glass above 1100°C and is suitable for industrial forming processes [60]. Upon further heating to approximately 150°C, the viscosity of ZnPIm-g decreases below the practical melting point ($\eta < 10$ Pa•s). In contrast, $ZnPIm_{0.8}ZrP_{0.2}$-g maintains viscosities above 10 Pa•s up to at least 160°C. For comparison, at 73°C, the working point of ZnPIm-g ($\eta = 10^3$ Pa•s), the viscosity of $ZnPIm_{0.8}ZrP_{0.2}$-g already reaches 2.2×10^5 Pa•s. This substantial enhancement in viscosity is consistent with the hypothesis that ZrP may act as a secondary network former, potentially promoting polymerization through additional phosphate coordination associated with Zr^{4+} species [14, 26]. However, this interpretation is based on macroscopic rheological behavior and does not constitute direct evidence for specific atomic-scale cross-linking. Comparable behavior has been reported in synthetically controlled MOGs with varying coordination-network sizes, where materials possessing more extended coordination networks exhibit significantly higher viscosity (4.0×10^4 Pa•s at 120°C) than their highly fragmented counterparts (0.68 Pa•s at 120°C) [14]. Similar trends have also been reported for Na_2O–Al_2O_3–SiO_2 glasses incorporating Al^{3+} as a secondary network former [26].

The supercooled liquid characteristics of ZnPIm-g and $ZnPIm_{0.8}ZrP_{0.2}$-g were compared with those of various reference materials using a fragility diagram (Figure 5D) [6, 41, 53–56]. The fragility indices (m) of ZnPIm-g and $ZnPIm_{0.8}ZrP_{0.2}$-g were estimated to be 83.0 ± 16.1 and 79.9 ± 16.2, respectively, with the values overlapping within experimental uncertainty. Compared with other systems, both materials exhibit higher fragility than inorganic $ZnCl_2$, with intermediate fragility (m = 23) [61], and show fragility comparable to that of the metallic glass $Pt_{60}Ni_{15}P_{25}$ (m = 67.2) [55]. Relative to previously reported MOGs, the fragility indices of ZnPIm-g and $ZnPIm_{0.8}ZrP_{0.2}$-g fall between $Zn(imidazolate)_{1.75}(benzimidazolate)_{0.25}$ (ZIF-62) [6], with an exceptionally low m of 23, and the relatively fragile $[Zn_3(H_2PO_4)_6(H_2O)_3]$(1,2,3-benzotriazole) ($m$ = 124) [24].

2.5 | Anhydrous Proton Conductivity

The proton conductivities of ZnPIm-g, $ZnPIm_{0.8}ZrP_{0.2}$-g, and $ZnPIm_{0.5}ZrP_{0.5}$-g were compared under anhydrous conditions, representing the pristine MOG, a modified sample with a homogeneous ZrP distribution, and a modified sample exhibiting clear phase segregation, respectively. All samples, in their molten states, were loaded into a conductivity cell of fixed geometry. Conductivity measurements were carried out by alternating current (AC) impedance spectroscopy (Figures S78 and S79). Each sample was equilibrated at the target temperature for at least 3 h prior to measurement, and all experiments were performed under a dry Ar atmosphere to maintain anhydrous conditions. Note that the temperature range used for proton conductivity measurements also covers temperatures above T_g for both materials, where they behave as highly viscous supercooled liquids.

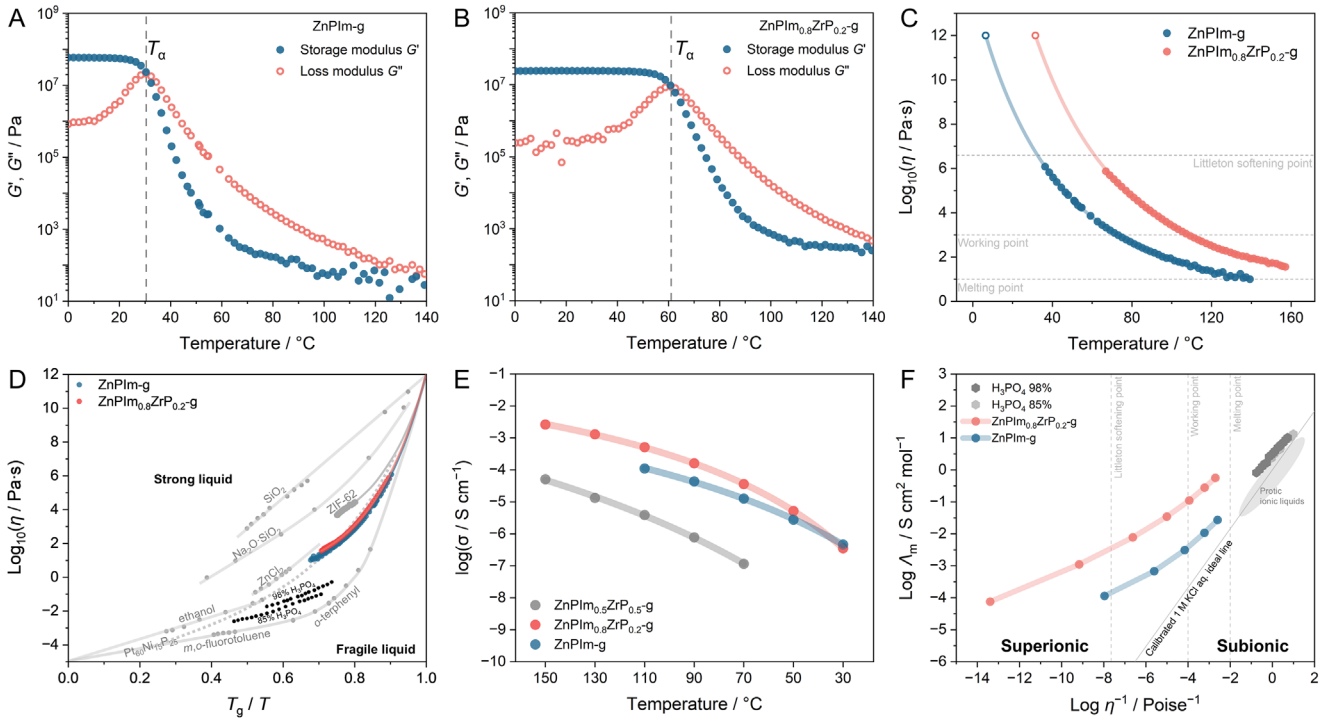

FIGURE 5 | Viscoelasticity and anhydrous proton conductivity of melt-quenched samples. Temperature-dependent storage modulus (G') and loss modulus (G'') of (A) ZnPIm-g and (B) $ZnPIm_{0.8}ZrP_{0.2}$-g measured at 1 Hz, 0.02% strain, and a cooling rate of 2°C min^{-1}. (C) Temperature-dependent viscosity of ZnPIm-g and $ZnPIm_{0.8}ZrP_{0.2}$-g. (D) Fragility plot of ZnPIm-g and $ZnPIm_{0.8}ZrP_{0.2}$-g in comparison with reference compounds. Data are reproduced from ref. [6, 41, 53–56]. (E) Variable-temperature proton conductivity of ZnPIm-g, $ZnPIm_{0.8}ZrP_{0.2}$-g, and $ZnPIm_{0.5}ZrP_{0.5}$-g under a dry Ar atmosphere. Data for ZnPIm-g are reproduced from ref. [23]. Fitting parameters are available in Tables S6 and S7. Conductivity values and errors are available in Table S8. (F) Walden plots of ZnPIm-g and $ZnPIm_{0.8}ZrP_{0.2}$-g compared with 85% and 98% H_3PO_4, and representative protic ionic liquids. Reference data of H_3PO_4, protic ionic liquids, and the calibrated ideal KCl line are taken from Ref. [54, 57].

The temperature-dependent proton conductivity of pristine ZnPIm-g follows Vogel–Fulcher–Tammann (VFT)-type behavior [62–64], exhibiting a maximum proton conductivity of 1.1×10^{-4} S cm^{-1} at 110°C (Figure 5E) [23]. Above this temperature, reliable measurements could not be obtained because the viscosity of ZnPIm-g decreases below its physical melting point, leading to sample leakage from the measurement setup. Incorporation of a small amount of ZrP in $ZnPIm_{0.8}ZrP_{0.2}$-g increases the proton conductivity by nearly five-fold compared to ZnPIm-g at 110°C, reaching 5.1×10^{-4} S cm^{-1}. Upon further heating to 150°C, the conductivity value of $ZnPIm_{0.8}ZrP_{0.2}$-g reaches a maximum at 2.6×10^{-3} S cm^{-1}. In contrast, $ZnPIm_{0.5}ZrP_{0.5}$-g exhibits significantly lower proton conductivity, 3.9×10^{-6} S cm^{-1} at 110°C and 5.1×10^{-5} S cm^{-1} at 150°C. This reduction in conductivity is consistent with the phase segregation observed in SEM/EDX analyses, which reveal the formation of ZrP-rich domains. These domains likely disrupt the continuity of the proton-conducting network, particularly given the relatively low intrinsic proton conductivity of ZrP. For example, $Zr(PO_4)(H_2PO_4)\cdot 2H_2O$ (γ-ZrP) exhibits anhydrous proton conductivity of 8×10^{-8} S cm^{-1} at 180°C [65]. Although the maximum conductivity achieved in the present work remains below the benchmark value required for practical applications (10^{-2} S cm^{-1}) [66], the enhanced proton conductivity of $ZnPIm_{0.8}ZrP_{0.2}$-g is achieved without a decrease in T_g or viscosity relative to pristine ZnPIm-g (Table S9). Future improvements in proton conductivity may be realized by replacing the parent MOG and/or the additive with components that exhibit higher intrinsic proton conductivity.

All three examples display VFT-type temperature dependence, indicating that proton transport is coupled to structural dynamics and facilitated by structural relaxation, a behavior characteristic of glassy or polymeric ion conductors [59]. This differs from Arrhenius-type behavior, typically associated with thermally activated hopping of charge carriers in crystalline conductors. The VFT fitting parameters are summarized in Table S10. The activation factor (B) decreases in the order $ZnPIm_{0.5}ZrP_{0.5}$-g (5423 K) > ZnPIm-g (2626 K) > $ZnPIm_{0.8}ZrP_{0.2}$-g (1725 K), indicating progressively weaker temperature dependence and lower apparent activation energies for proton conduction [59, 67].

The relationship between viscosity (η) and equivalent conductivity (Λ_m) of ZnPIm-g and $ZnPIm_{0.8}ZrP_{0.2}$-g was examined using a Walden plot to elucidate the underlying proton-conductivity mechanisms (Figure 5F) [68, 69]. Along Walden's ideal line, conductivity is directly proportional to fluidity, indicating that ion migration is fully coupled to the viscous flow of the medium, a characteristic of dilute fluid systems where ion transport follows the vehicle mechanism [59]. In our study, both samples fall within the superionic region, deviating substantially from Walden's ideal line. Such deviations indicate that charge carriers are partially decoupled from the matrix dynamics and that proton transport is governed predominantly by the Grotthuss mechanism rather than viscous diffusion. For reference, phosphoric acid, which is located slightly above Walden's ideal line, exhibits ~97% of its proton conductivity via the Grotthuss mechanism [59, 70].

In our systems, the coordination networks within the MOG framework likely restrict counter-ion mobility while facilitating proton hopping along interconnected hydrogen-bond pathways [14, 71]. Compared with the pristine ZnPIm-g, $ZnPIm_{0.8}ZrP_{0.2}$-g shows a larger deviation from Walden's ideal line toward the superionic region. This shift reflects its higher viscosity and enhanced proton conductivity, implying weaker coupling between structural relaxation and proton transport. $ZnPIm_{0.8}ZrP_{0.2}$-g maintains a broader viscoelastic proton-conducting regime than ZnPIm-g before transforming into a viscous liquid upon surpassing the working-point threshold (log $\eta^{-1} = -4$ Poise^{-1}) [56]. These observations support our hypothesis that ZrP incorporation introduces additional phosphate sites that improve hydrogen-bond connectivity, thereby stabilizing dynamic proton-conducting pathways and promoting long-range transport.

3 | Conclusion

This study presents a strategy to modulate the properties of MOGs through the incorporation of amorphous ZrP, which is hypothesized to act as a secondary network former. We demonstrate that ZrP significantly influences the glassy-state properties of proton-conductive ZnPIm, enabling controlled tuning of the glass transition temperature, viscoelasticity, and anhydrous proton conductivity. By systematically varying the amount of ZrP, a linear increase in T_g from 11.0°C to 57.4°C is achieved, together with anhydrous proton conductivities up to 2.6×10^{-3} S cm^{-1} at 150°C and over two orders of magnitude enhancement in viscosity at 73°C relative to the pristine MOG. Synchrotron X-ray total scattering and PDF analyses indicate preservation of short-range metal–ligand–metal connectivity in the glassy state, while both metal centers retain their characteristic coordination geometries. On the basis of these macroscopic thermal and rheological trends, we envisage that ZrP functions as a secondary network-forming component that promotes increased polymerization within the coordination network, analogous to the role of intermediate or network-forming oxides in conventional silicate glasses. Direct microscopic experimental evidence for this cross-linking mechanism is not provided in the present work and remains an important topic for future investigation. Overall, this work establishes a foundation for the compositional design of hybrid glasses, bridging the principles from oxide glass science and coordination chemistry to enable new routes for tailoring the structure, thermal behavior, and functional properties of MOGs.

Acknowledgements

N.M. acknowledges the support from ICYS for a research fellowship, from the JST PRESTO grant JPMJPR25MB, from JSPS KAKENHI Grant Numbers JP24K23109 and JP25K18055, from the Sumitomo Foundation basic science grant number 2402150, and from the Iketani Science and Technology Foundation grant number 0371207-A. We acknowledge the BL04B2 beamlines at SPring-8 for the synchrotron X-ray total scattering experiments with the approval of JASRI (Proposal Numbers 2024B1167, 2025A1067, and 2025B1248). This work was supported by the World Premier International Research Center Initiative (WPI), MEXT, Japan. We acknowledge support from Dr. Hiroki Yamada (SPring-8) and Dr. Soracha Kosasang (NIMS) during the X-ray total scattering measurement. We acknowledge Dr. Soracha Kosasang (NIMS) for high-temperature TGA measurements. We thank Dr. Shinsuke Ishihara (NIMS) for providing access to FTIR. We acknowledge support from the NIMS Surface and Bulk Analysis Unit and NIMS Nanofabrication Facilities.

Conflicts of Interest

The authors declare no conflict of interest.

Data Availability Statement

The data that support the findings of this study are available from the corresponding author upon reasonable request.

References

1. D. Umeyama, S. Horike, M. Inukai, T. Itakura, and S. Kitagawa, "Reversible Solid-to-Liquid Phase Transition of Coordination Polymer Crystals," *Journal of the American Chemical Society* 137 (2015): 864–870, https://doi.org/10.1021/ja511019u.

2. T. D. Bennett, J.-C. Tan, Y. Yue, et al., "Hybrid Glasses From Strong and Fragile Metal-Organic Framework Liquids," *Nature Communications* 6 (2015): 8079, https://doi.org/10.1038/ncomms9079.

3. Y. Hirai, T. Nakanishi, Y. Kitagawa, et al., "Luminescent Coordination Glass: Remarkable Morphological Strategy for Assembled Eu(III) Complexes," *Inorganic Chemistry* 54 (2015): 4364–4370.

4. N. Ma and S. Horike, "Metal–Organic Network-Forming Glasses," *Chemical Reviews* 122 (2022): 4163–4203.

5. N. Ma, S. Kosasang, E. K. Berdichevsky, T. Nishiguchi, and S. Horike, "Functional Metal–organic Liquids," *Chemical Science* 15 (2024): 7474–7501.

6. A. Qiao, T. D. Bennett, H. Tao, et al., "A Metal-Organic Framework With Ultrahigh Glass-Forming Ability," *Science Advances* 4 (2018): aao6827, https://doi.org/10.1126/sciadv.aao6827.

7. L. Frentzel-Beyme, M. Kloß, P. Kolodzeiski, R. Pallach, and S. Henke, "Meltable Mixed-Linker Zeolitic Imidazolate Frameworks and Their Microporous Glasses: From Melting Point Engineering to Selective Hydrocarbon Sorption," *Journal of the American Chemical Society* 141 (2019): 12362–12371, https://doi.org/10.1021/jacs.9b05558.

8. T. D. Bennett and S. Horike, "Liquid, Glass and Amorphous Solid States of Coordination Polymers and Metal–Organic Frameworks," *Nature Reviews Materials* 3 (2018): 431–440, https://doi.org/10.1038/s41578-018-0054-3.

9. D. Umeyama, N. P. Funnell, M. J. Cliffe, et al., "Glass Formation via Structural Fragmentation of a 2D Coordination Network," *Chemical Communications* 51 (2015): 12728–12731, https://doi.org/10.1039/C5CC04626B.

10. W. Chen, S. Horike, D. Umeyama, et al., "Glass Formation of a Coordination Polymer Crystal for Enhanced Proton Conductivity and Material Flexibility," *Angewandte Chemie International Edition* 55 (2016): 5195–5200, https://doi.org/10.1002/anie.201600123.

11. Y. Ohara, A. Hinokimoto, W. Chen, et al., "Formation of Coordination Polymer Glass by Mechanical Milling: Dependence on Metal Ions and Molecular Doping for H^+ Conductivity," *Chemical Communications* 54 (2018): 6859–6862.

12. S. Kosasang, N. Ma, D. L. Christensen, M. M. Smedskjaer, H. Yamada, and S. Horike, "Metal–Organic Crystallized Glasses: Microstructure Formation and Their Properties," *Journal of the American Chemical Society* 147 (2025): 33870–33878.

13. F. Cao, S. S. Sørensen, A. K. R. Christensen, et al., "Continuous Structure Modification of Metal-organic Framework Glasses via Halide Salts," *Nature Communications* 16 (2025): 7001, https://doi.org/10.1038/s41467-025-62143-9.

14. T. Ogawa, K. Takahashi, T. Kurihara, et al., "Network Size Control in Coordination Polymer Glasses and Its Impact on Viscosity and H^+ Conductivity," *Chemistry of Materials* 34 (2022): 5832–5841.

15. M. Kim, H.-S. Lee, D.-H. Seo, S. J. Cho, E. Jeon, and H. R. Moon, "Melt-quenched Carboxylate Metal–Organic Framework Glasses," *Nature Communications* 15 (2024): 1174.

16. J. Hou, P. Chen, A. Shukla, et al., "Liquid-Phase Sintering of Lead Halide Perovskites and Metal-organic Framework Glasses," *Science* 374 (2021): 621–625, https://doi.org/10.1126/science.abf4460.

17. L. León-Alcaide, L. Martínez-Goyeneche, M. Sessolo, et al., "Direct Synthesis of an Iron Metal-Organic Framework Antiferromagnetic Glass," *Nature Communications* 16 (2025): 8783, https://doi.org/10.1038/s41467-025-63837-w.

18. W.-L. Xue, P. Kolodzeiski, H. Aucharova, S. Vasa, et al., "Highly Porous Metal-organic Framework Liquids and Glasses via a Solvent-Assisted Linker Exchange Strategy of ZIF-8," *Nature Communications* 15 (2024): 4420, https://doi.org/10.1038/s41467-024-48703-5.

19. S. Kohara, K. Suzuya, K. Takeuchi, et al., "Glass Formation at the Limit of Insufficient Network Formers," *Science* 303 (2004): 1649–1652, https://doi.org/10.1126/science.1095047.

20. Y. Onodera, S. Kohara, H. Masai, A. Koreeda, S. Okamura, and T. Ohkubo, "Formation of Metallic Cation-oxygen Network for Anomalous Thermal Expansion Coefficients in Binary Phosphate Glass," *Nature Communications* 8 (2017): 15449, https://doi.org/10.1038/ncomms15449.

21. S. M. Wiederhorn and D. R. Clarke, "Architectural Glass," *Annual Review of Materials Research* 52 (2022): 561–592, https://doi.org/10.1146/annurev-matsci-101321-014417.

22. I. W. Donald, B. L. Metcalfe, and R. N. J. Taylor, "The Immobilization of High Level Radioactive Wastes Using Ceramics and Glasses," *Journal of Materials Science* 32 (1997): 5851–5887, https://doi.org/10.1023/A:1018646507438.

23. N. Ma, N. Horike, L. Lombardo, et al., "Eutectic $CsHSO_4$-Coordination Polymer Glasses With Superprotonic Conductivity′," *Journal of the American Chemical Society* 144 (2022): 18619–18628.

24. N. Ma, S. Kosasang, S. Horike, and H. Yamada, "Liquid Coordination Polymers With Anhydrous Proton Conductivity," *Angewandte Chemie International Edition* 64 (2025): 202504618, https://doi.org/10.1002/anie.202504618.

25. S. S. Sørensen, X. Ren, T. Du, et al., "Water as a Modifier in a Hybrid Coordination Network Glass," *Small* 19 (2023): 2205988.

26. C. Le Losq, D. R. Neuville, P. Florian, G. S. Henderson, and D. Massiot, "The Role of Al^{3+} on Rheology and Structural Changes in Sodium Silicate and Aluminosilicate Glasses and Melts," *Geochimica et Cosmochimica Acta* 126 (2014): 495–517.

27. N. Ma, S. Impeng, S. Bureekaew, N. Morozumi, M. Haga, and S. Horike, "Photoexcited Anhydrous Proton Conductivity in Coordination Polymer Glass," *Journal of the American Chemical Society* 145 (2023): 9808–9814, https://doi.org/10.1021/jacs.3c01821.

28. X. Zheng, K. Nagura, T. Takaya, K. Hashi, and T. Nakanishi, "Quest for a Rational Molecular Design of Alkyl-Distyrylbenzene Liquid by Substitution Pattern Modulation," *Chemistry – A European Journal* 29 (2023): 202203775.

29. M. A. Salvadó, P. Pertierra, S. García-Granda, L. M. Barcina, R. Llavona, and J. Rodríguez, "Hydrogen Bond Network of the Layered Phosphates γ-$Zr(H_2PO_4)(PO_4)\,2H_2O$ and γ-$Hf(H_2PO_4)(PO_4)\,2H_2O$ Determined by Neutron Powder Diffraction," *Zeitschrift für Kristallographie-Crystalline Materials* 216 (2001): 326–330.

30. D. E. Harrison, H. A. McKinstry, and F. A. Hummel, "High-Temperature Zirconium Phosphates," *Journal of the American Ceramic Society* 37 (1954): 277–288, https://doi.org/10.1111/j.1151-2916.1954.tb14037.x.

31. G. Wallez, J.-P. Souron, and M. Quarton, "Crystal Structure and Thermal Evolution of Inedite α-$Zr_2O(PO_4)_2$ and α-$Hf_2O(PO_4)_2$," *Solid State Sciences* 8 (2006): 1061–1066, https://doi.org/10.1016/j.solidstatesciences.2006.02.054.

32. J. F. Willart, A. De Gusseme, S. Hemon, G. Odou, F. Danede, and M. Descamps, "Direct Crystal to Glass Transformation of Trehalose Induced by Ball Milling," *Solid State Communications* 119 (2001): 501–505, https://doi.org/10.1016/S0038-1098(01)00283-6.

33. E. Ma, "Amorphization in Mechanically Driven Material Systems," *Scripta Materialia* 49 (2003): 941–946, https://doi.org/10.1016/S1359-6462(03)00477-9.

34. J. F. Willart and M. Descamps, "Solid State Amorphization of Pharmaceuticals," *Molecular Pharmaceutics* 5 (2008): 905–920, https://doi.org/10.1021/mp800092t.

35. Z. Guo, C. Pan, A. Shinohara, and T. Nakanishi, "Merging π-molecular Functions Achieved Through Homogeneous Liquid-Liquid Blending of Solvent-free Alkyl-π Liquids," *Science and Technology of Advanced Materials* 26 (2025): 2515007, https://doi.org/10.1080/14686996.2025.2515007.

36. K. Ito, C. T. Moynihan, and C. A. Angell, "Thermodynamic Determination of Fragility in Liquids and a Fragile-to-Strong Liquid Transition in Water," *Nature* 398 (1999): 492–495, https://doi.org/10.1038/19042.

37. G. N. Greaves and S. Sen, "Inorganic Glasses, Glass-forming Liquids and Amorphizing Solids," *Advances in Physics* 56 (2007): 1–166, https://doi.org/10.1080/00018730601147426.

38. L. Longley, S. M. Collins, C. Zhou, et al., "Liquid Phase Blending of Metal-Organic Frameworks," *Nature Communications* 9 (2018): 2135, https://doi.org/10.1038/s41467-018-04553-6.

39. C. Thanaphatkosol, N. Ma, K. Kageyama, et al., "Modulation of Proton Conductivity in Coordination Polymer Mixed Glasses," *Chemical Communications* 58 (2022): 6064–6067, https://doi.org/10.1039/D2CC01266A.

40. L. Longley, C. Calahoo, R. Limbach, et al., "Metal-organic Framework and Inorganic Glass Composites," *Nature Communications* 11 (2020): 5800, https://doi.org/10.1038/s41467-020-19598-9.

41. C. A. Angell, "Formation of Glasses From Liquids and Biopolymers," *Science* 267 (1995): 1924–1935, https://doi.org/10.1126/science.267.5206.1924.

42. S. J. Tao, "Positronium Annihilation in Molecular Substances," *The Journal of Chemical Physics* 56 (1972): 5499–5510, https://doi.org/10.1063/1.1677067.

43. C. Hugenschmidt, U. Holzwarth, M. Jansen, S. Kohn, and K. Maier, "Crystallization of Silica Studied by Positron Annihilation," *Journal of Non-Crystalline Solids* 217 (1997): 72–78, https://doi.org/10.1016/S0022-3093(97)00104-X.

44. J. C. Machado, G. G. Silva, and L. S. Soares, "Positron Annihilation and Differential Scanning Calorimetry Investigations in Poly(methylmethacrylate)/Low Molecular Weight Poly(ethylene oxide) Polymer Blends," *Journal of Polymer Science Part B: Polymer Physics* 38 (2000): 1045–1052, https://doi.org/10.1002/(SICI)1099-0488(20000415)38:8%3c1045::AID-POLB5%3e3.0.CO;2-N.

45. A. J. Hill, M. D. Zipper, M. R. Tant, G. M. Stack, T. C. Jordan, and A. R. Shultz, "A Free Volume Approach to the Mechanical Behaviour of Miscible Polycarbonate Blends," *Journal of Physics-Condensed Matter* 8 (1996): 3811.

46. M. W. Terban and S. J. L. Billinge, "Structural Analysis of Molecular Materials Using the Pair Distribution Function," *Chemical Reviews* 122 (2022): 1208–1272, https://doi.org/10.1021/acs.chemrev.1c00237.

47. S. Horike, D. Umeyama, M. Inukai, T. Itakura, and S. Kitagawa, "Coordination-Network-Based Ionic Plastic Crystal for Anhydrous Proton Conductivity," *Journal of the American Chemical Society* 134 (2012): 7612–7615, https://doi.org/10.1021/ja301875x.

48. C. L. Farrow, P. Juhas, J. W. Liu, et al., "PDFfit2 and PDFgui: Computer Programs for Studying Nanostructure in Crystals," *Journal of Physics-Condensed Matter* 19 (2007): 335219.

49. T. L. Christiansen, S. R. Cooper, and K. M. Ø. Jensen, "There's no Place Like Real-Space: Elucidating Size-Dependent Atomic Structure of

Nanomaterials Using Pair Distribution Function Analysis," *Nanoscale Advances* 2 (2020): 2234–2254, https://doi.org/10.1039/D0NA00120A.

50. A. Sutrisno, L. Liu, J. Dong, and Y. Huang, "Solid-State ^{91}Zr NMR Characterization of Layered and Three-Dimensional Framework Zirconium Phosphates′," *The Journal of Physical Chemistry* 116 (2012): 17070–17081.

51. J. Qiao, J.-M. Pelletier, and R. Casalini, "Relaxation of Bulk Metallic Glasses Studied by Mechanical Spectroscopy," *The Journal of Physical Chemistry B* 117 (2013): 13658–13666, https://doi.org/10.1021/jp4067179.

52. R. H. Colby, L. J. Fetters, and W. W. Graessley, "The Melt Viscosity-molecular Weight Relationship for Linear Polymers," *Macromolecules* 20 (1987): 2226–2237, https://doi.org/10.1021/ma00175a030.

53. C. A. Angell, C. T. Moynihan, and M. Hemmati, "'Strong' and 'Superstrong' Liquids, and an Approach to the Perfect Glass State via Phase Transition," *Journal of Non-Crystalline Solids* 274 (2000): 319–331, https://doi.org/10.1016/S0022-3093(00)00222-2.

54. J.-P. Belieres and C. A. Angell, "Protic Ionic Liquids: Preparation, Characterization, and Proton Free Energy Level Representation," *The Journal of Physical Chemistry B* 111 (2007): 4926–4937, https://doi.org/10.1021/jp067589u.

55. A. Takeuchi, H. Kato, and A. Inoue, "Vogel–Fulcher–Tammann Plot for Viscosity Scaled With Temperature Interval Between Actual and Ideal Glass Transitions for Metallic Glasses in Liquid and Supercooled Liquid States," *Intermetallics* 18 (2010): 406–411, https://doi.org/10.1016/j.intermet.2009.08.015.

56. U. Fotheringham, *Springer Handbook of Glass*, ed. J.D. Musgraves, J. Hu, and L. Calvez, (Springer International Publishing, 2019): 79–112.

57. C. Schreiner, S. Zugmann, R. Hartl, and H. J. Gores, "Fractional Walden Rule for Ionic Liquids: Examples From Recent Measurements and a Critique of the So-Called Ideal KCl Line for the Walden Plot," *Journal of Chemical & Engineering Data* 55 (2010): 1784–1788, https://doi.org/10.1021/je900878j.

58. J. C. Mauro, Y. Yue, A. J. Ellison, P. K. Gupta, and D. C. Allan, "Viscosity of Glass-Forming Liquids," *Proceedings of the National Academy of Sciences* 106 (2009): 19780–19784, https://doi.org/10.1073/pnas.0911705106.

59. Y. Wang, N. A. Lane, C.-N. Sun, F. Fan, T. A. Zawodzinski, and A. P. Sokolov, "Ionic Conductivity and Glass Transition of Phosphoric Acids," *The Journal of Physical Chemistry B* 117 (2013): 8003–8009, https://doi.org/10.1021/jp403867a.

60. J. E. Shelby, *Introduction to Glass Science and Technology* (Royal Society Of Chemistry, 2005), https://doi.org/10.1039/9781847551160.

61. P. Lucas, G. J. Coleman, M. Venkateswara Rao, et al., "Structure of ZnCl 2 Melt. Part II: Fragile-to-Strong Transition in a Tetrahedral Liquid," *The Journal of Physical Chemistry B* 121 (2017): 11210–11218, https://doi.org/10.1021/acs.jpcb.7b10857.

62. H. Vogel, "The Law of the Relation Between the Viscosity of Liquids and the Temperature," *J Phys Z* 22 (1921): 645–646.

63. G. S. Fulcher, "Analysis of Recent Measurements of the Viscosity of Glasses," *Journal of the American Ceramic Society* 8 (1925): 339–355, https://doi.org/10.1111/j.1151-2916.1925.tb16731.x.

64. G. Tammann and W. Hesse, "Die Abhängigkeit der Viscosität von der Temperatur bie unterkühlten Flüssigkeiten," *Zeitschrift für anorganische und allgemeine Chemie* 156 (1926): 245–257, https://doi.org/10.1002/zaac.19261560121.

65. G. Alberti, M. G. Bernasconi, and M. Casciola, "Preparation of γ-zirconium Phosphate Microcrystals With High Degree of Crystallinity and Proton Conductivity of Their Hydrogen and Ammonium Forms," *Reactive Polymers* 11 (1989): 245–252, https://doi.org/10.1016/0923-1137(89)90110-3.

66. B. C. H. Steele and A. Heinzel, "Materials for Fuel-cell Technologies," *Nature* 414 (2001): 345–352, https://doi.org/10.1038/35104620.

67. M. A. B. H. Susan, T. Kaneko, A. Noda, and M. Watanabe, "Ion Gels Prepared by in Situ Radical Polymerization of Vinyl Monomers in an Ionic Liquid and Their Characterization as Polymer Electrolytes," *Journal of the American Chemical Society* 127 (2005): 4976–4983, https://doi.org/10.1021/ja045155b.

68. C. Austen Angell, Y. Ansari, and Z. Zhao, "Ionic Liquids: Past, Present and Future," *Faraday Discussions* 154 (2012): 9–27, https://doi.org/10.1039/C1FD00112D.

69. W. Xu and C. A. Angell, "Solvent-Free Electrolytes With Aqueous Solution-Like Conductivities," *Science* 302 (2003): 422–425, https://doi.org/10.1126/science.1090287.

70. J.-P. Melchior, K.-D. Kreuer, and J. Maier, "Proton Conduction Mechanisms in the Phosphoric Acid–Water System ($H_4P_2O_7$–H_3PO_4·$2H_2O$): a ^{1}H, ^{31}P and ^{17}O PFG-NMR and Conductivity Study,"*Physical Chemistry Chemical Physics* 19 (2017): 587–600.

71. T. Ogawa, K. Takahashi, S. S. Nagarkar, et al., "Coordination Polymer Glass From a Protic Ionic Liquid: Proton Conductivity and Mechanical Properties as an Electrolyte," *Chemical Science* 11 (2020): 5175–5181, https://doi.org/10.1039/D0SC01737J.

Supporting Information

Additional supporting information can be found online in the Supporting Information section.

Supporting File: smll72859-sup-0001-SuppMat.pdf.